Scientific Reports

https://doi.org/10.1038/s41598-026-42857-6

Article in Press

Advanced smartwatch for noninvasive sweat biomarker monitoring using a wearable FET biosensor array with Ag nanowire cross-linked MoS_2 and MXene

Received: 24 May 2025

Accepted: 27 February 2026

Published online: 20 May 2026

Cite this article as: Farahmandpour M., Dideban D., Dehbali M.M. *et al.* Advanced smartwatch for noninvasive sweat biomarker monitoring using a wearable FET biosensor array with Ag nanowire cross-linked MoS_2 and MXene. *Sci Rep* (2026). https://doi.org/10.1038/s41598-026-42857-6

Milad Farahmandpour, Daryoosh Dideban, Masoomeh Monfared Dehbali & Zoheir Kordrostami

Advanced smartwatch for noninvasive sweat biomarker monitoring using a wearable FET biosensor array with Ag nanowire cross-linked MoS_2 and MXene

Milad Farahmandpour[1], Daryoosh Dideban[1*], Masoomeh Monfared Dehbali[2,3], Zoheir Kordrostami[2,3]

[1]Department of Electrical and Computer Engineering, University of Kashan, Kashan, Iran
[2]Department of Electrical and Electronic Engineering, Shiraz University of Technology, Shiraz, Iran
[3]Research Center for Design and Fabrication of Advanced Electronic Devices, Shiraz University of Technology, Shiraz, Iran
[*]**Corresponding Author: dideban@kashanu.ac.ir**

Abstract

This study introduces the development of a next-generation wearable biosensor for non-invasive glucose monitoring in human sweat, leveraging the unique properties of advanced two-dimensional (2D) nanomaterials. Central to this innovation is a smartwatch-based platform designed for real-time health monitoring. The research focuses on three distinct field-effect transistor (FET) configurations, each utilizing a copper electrode array as the source, drain, and gate, and different 2D composite materials as the transistor channel. The FET channels were fabricated using a hydrothermal synthesis method to produce four high-performance composites: silver nanowires/Ti_3C_2 MXene, Ti_3C_2 MXene/MoS_2, AgNWs/MoS_2. and a ternary combination of MoS_2/Ti_3C_2 MXene/silver nanowires. Each material contributes unique advantages—silver nanowires provide high electrical conductivity for efficient charge transport, MoS_2 provides abundant active sites for glucose oxidation, and Ti_3C_2 MXene enhances both electrical conductivity and surface functionalization, facilitating improved glucose detection. In addition to glucose sensing, the developed smartwatch can simultaneously monitor pH and temperature, factors that are critical for accurate biosensing in sweat. Comprehensive material analysis, fabrication methods, and performance evaluations are detailed in this work. The proposed Bio-FET sensors demonstrate outstanding performance metrics, including an ultra-low detectable concentration of 0.001 µM , a sensitivity of 355 $mA \cdot mM^{-1}$, and a broad span of linear detection from 0 to 10 mM. The sensors also exhibit excellent repeatability, reproducibility, and long-term stability.

Keywords: Wearable FET array, Smart Watch, Sweat sensors, Ag Nanowires, MoS_2, Ti_3C_2 MXene.

Introduction

Wearable and flexible FET biosensors have garnered significant attention due to their ability to accurately and non-invasively detect biomarkers. Among various biofluids, sweat is particularly advantageous for real time biomarker monitoring since it can be easily sampled on the body, providing quick insights into physical health conditions. Sweat-sensing devices, however, face difficulties in real-time sampling and necessitate a sensing platform that is extremely sensitive, selective, and long-term stable, notwithstanding its potential. Additionally, the readings from these biosensors can be influenced by fluctuations in sweat pH, temperature, and other physicochemical factors. Skin sweat exhibits variable pH (4.5–7), which can change with exercise and environmental conditions, affecting biomarker measurements. Temperature variations can also significantly impact enzyme activity in enzymatic sensors. Therefore, integrating FET sensors that can monitor pH and temperature into a smart watch platform is essential for calibrating biomarker measurements and enhancing accuracy[1-9].

The integration of MoS_2, Ti_3C_2 MXene, and silver (Ag) nanowires in glucose sensing platforms show significant promise due to their unique electrical and electrochemical properties. MoS_2, a transition metal dichalcogenide, offers excellent conductivity, high electrocatalytic activity and a large surface area, enhancing the sensor's sensitivity. Ti_3C_2 MXenes, known for their high conductivity and tunable surface chemistry, improve charge transfer kinetics, facilitating rapid glucose detection. Meanwhile, Ag nanowires provide an excellent conductive pathway and increase the electrocatalytic activity at the sensing interface[10-13]. Together, these materials create a synergistic effect, resulting in highly sensitive and selective glucose sensors, which are critical for real-time monitoring in diabetes management.

BioFET sensor array for detecting biomarkers in sweat offer several advantages, including their non-invasive nature, which allows for real-time monitoring without the discomfort of blood sampling. They enable the simultaneous detection of multiple biomarkers, providing comprehensive health insights. Additionally, these sensors can operate at low analyte concentrations, enhancing sensitivity and specificity. Their integration into wearable technology facilitates continuous monitoring, making them ideal for applications in sports, health tracking, and personalized medicine. Overall, BioFET sensor array present a promising approach for advancing biomarker detection in a convenient and efficient manner[13-18].

Reduced graphene oxide integrated with PEDOT:PSS has emerged as a promising structure for wearable temperature sensor applications. This composite offers from the electrical properties of rGO and the advantageous characterizations of PEDOT:PSS, causing in improved sensitivity and flexibility. The rGO/PEDOT:PSS sensors can conform to various surfaces, including skin, allowing for accurate and real-time temperature monitoring. Their lightweight and stable nature, along with the potential for low-cost production, makes them ideal for integration into wearable devices for health and wellness monitoring[19-22].

Smartwatches connected to mobile devices and equipped with a FET sensor array for sweat biomarker detection offer numerous advantages. This setup enables continuous, real-time monitoring of health metrics without invasive procedures, enhancing user convenience and

compliance. The integration of FET sensors allows for highly sensitive and selective detection of various biomarkers, providing valuable insights into pH levels and glucose concentrations. Moreover, the connectivity with mobile devices facilitates immediate data analysis and user feedback, empowering individuals to make informed health decisions. This combination of wearable technology and advanced sensing enhances overall wellness monitoring, making it a compelling solution for proactive health management[23].

This study presents a long-term stable smartwatch platform that utilizes FET sensors with channels composed of MoS_2 nanosheets supported on Ti_3C_2 MXene and cross-linked by silver Ag nanowires for highly sensitive, selective, and accurate biomarker monitoring. The proposed platform features three sensors for measuring glucose, pH, and temperature. In addition to improved sensitivity, the FET sensor array provides a robust and effective platform for simultaneous measurement of both glucose and pH. When integrated with a temperature sensor, the smart watch can calibrate glucose readings by concurrently monitoring temperature and pH levels. Furthermore, the smartwatch is combined with a microfluidic channel for sweat sampling, demonstrating great promise for the accurate and continuous analysis of sweat under various conditions, which is essential for practical applications.

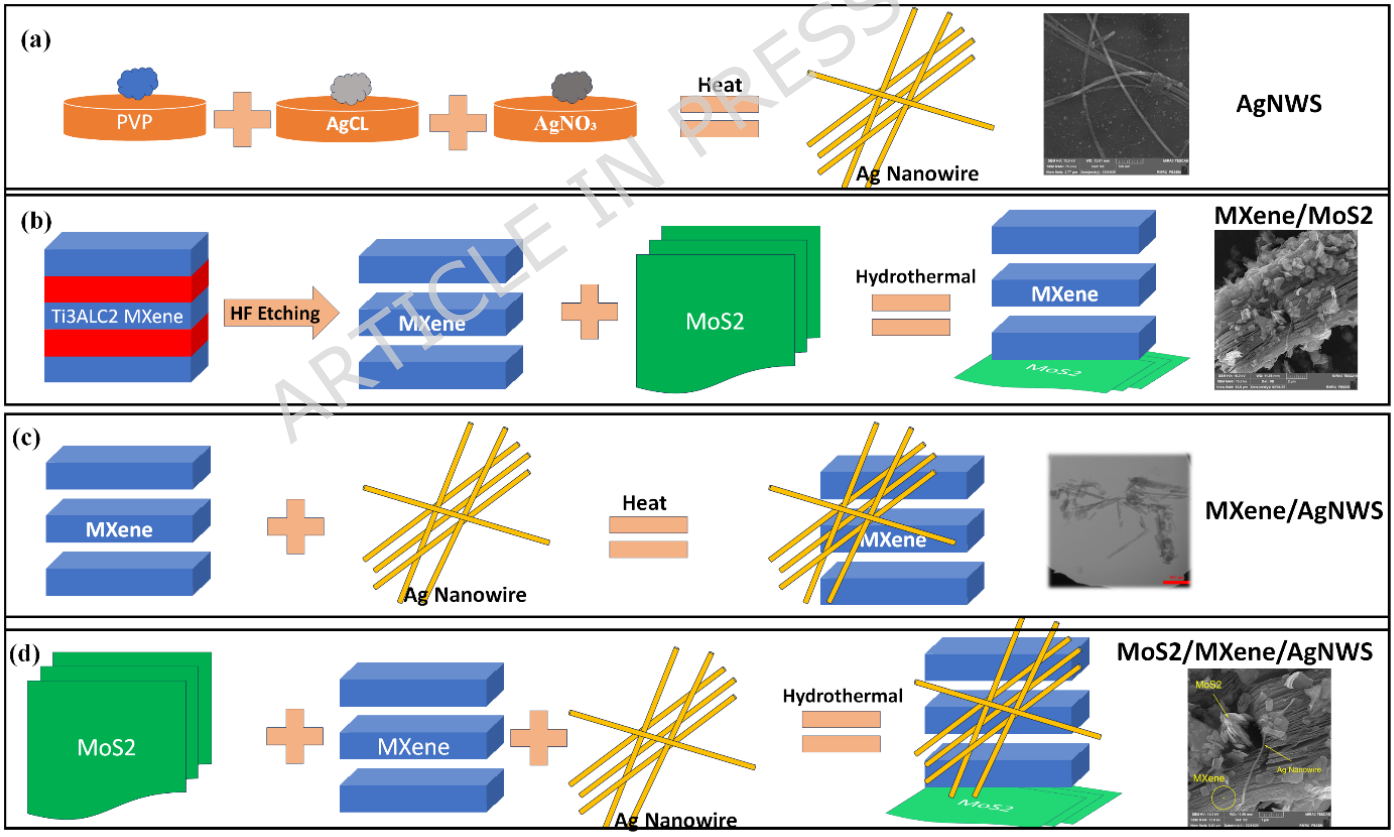

Fig1. A visual diagram depicting the methodology of the synthesis procedure of FET sensors channel material.

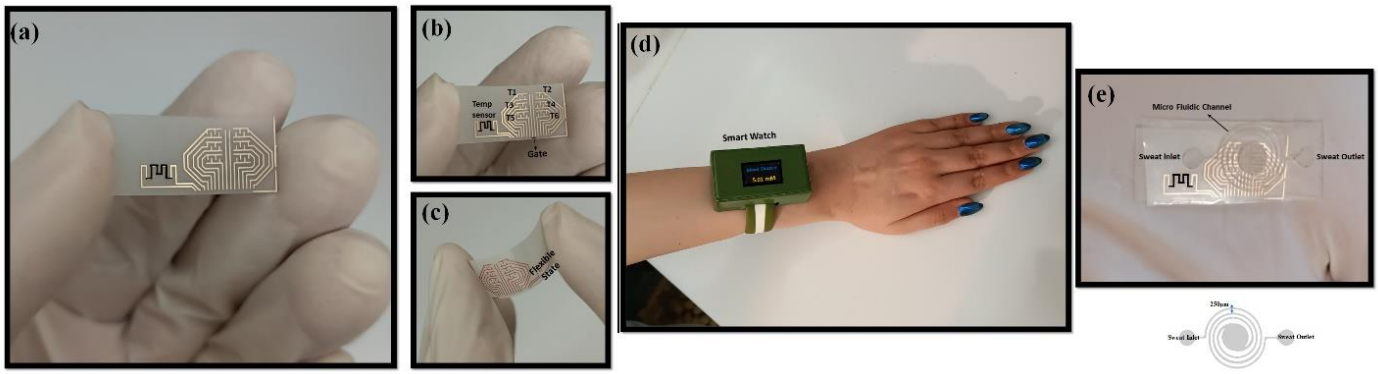

Fig2. Real images of **(a-c)** FET biosensors array, (d) smart watch, and (e) sensors integrated with microfluidic channel.

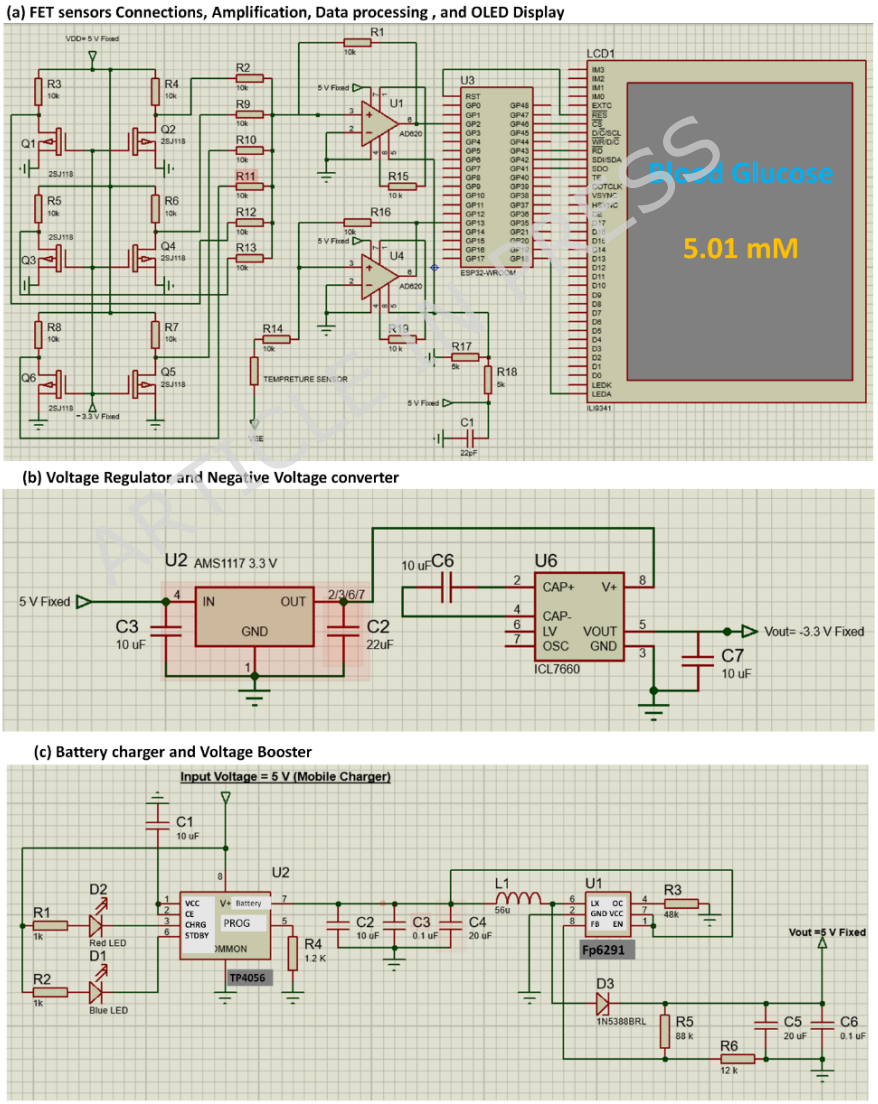

Fig3. Diagram of designed electrical current for smart watch.

Results and discussion

Material Characterization

The structural characteristics of MoS_2 nanosheets deposited on Ti_3C_2 MXene are shown **in Figures 4(a-c).** Unlike MoS_2 nanolayers, which typically manifest a flake shape and tend to form aggregated clusters, the 2D MoS_2 layers are seen growing within the interlayer spaces and on the outer layer of the Ti_3C_2 MXene. This sandwich-like structure of MoS_2 and Ti_3C_2 MXene—not only inhibits the restacking of the two-dimensional layers while also acting as a barrier for the Ti_3C_2 MXene from oxidation. As shown in **Figure 4d**, the silver nanowires are depicted, while **Figures 4(e) and (f)** illustrate the overall morphology of the AgNWs/Ti_3C_2 MXene/MoS_2 composite, where the three constituents are distinctly identifiable. This composite possesses a three-part architecture that combines hybrid arrangements of one-dimensional and two-dimensional structures. Additionally, the silver nanowires serve as connecting bridges between the 2D MoS_2 and Ti_3C_2 MXene islands, promoting the development of a continuous and efficient conductive framework that significantly improves charge movement across the material. TEM images of Ti_3C_2 MXene/AgNW are presented in **Figure 5a**, which displays a binary composite consisting of 1D and 2D hybrid structures. **Figure 5(b,c)** depict the TEM images of MoS_2/ Ti_3C_2 MXene, illustrating that MoS_2 nanosheets are deposited on Ti_3C_2 MXene. The TEM images of the MoS_2/AgNWs/ Ti_3C_2 MXene ternary composite are shown in **Figures 5(d-f)**. Although the density of AgNWs is relatively low, they act as bridges between the two-dimensional islands, they facilitate the development of a seamless, interconnected conductive pathway, greatly improving electron transport across the entire system.

The Ti_3C_2 MXene enhances surface functionalization by providing abundant, readily accessible terminal groups (e.g., –OH and –O) on its surface after mild etching, which serve as active sites for subsequent chemical modifications and biomolecule attachment; additionally, the high surface area and farmwork network formed by Ti_3C_2 MXene facilitate more uniform functionalization and improved electron transfer to the bifunctional layer, thereby increasing the effective surface reactivity and sensor response[24,25].

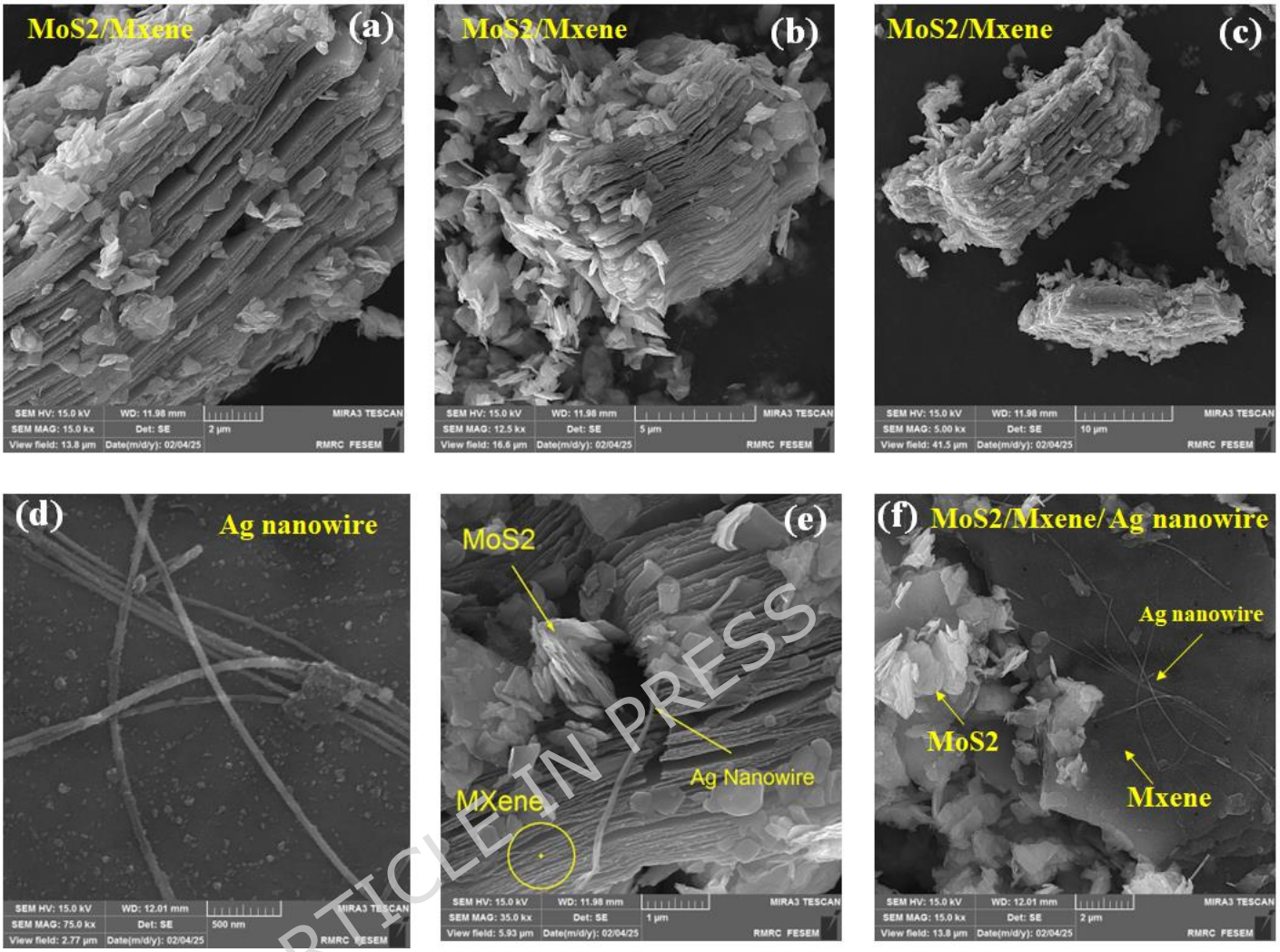

Fig.4. FESEM micrographs of (a-c) Ti_3C_2 MXene/MoS_2, (d) Ag nanowires, (e,f) Ti_3C_2 MXene/ MoS_2/Ag nanowires.

The elemental distribution indicated in **Figure 6's** EDS mapping demonstrates a consistent spread of molybdenum (Mo), sulfur (S), titanium (Ti), oxygen (O), fluorine (F), silver (Ag), and carbon (C). The EDX spectrum in **Figures 6(a–j)** reveals prominent peaks for Mo and Ti, complemented by the FESEM image of the analyzed area. Furthermore, the EDX tables and the spectrum in Figures **6(k,l)** detail the atomic and weight percentages of all involved elements, providing a comprehensive compositional overview.

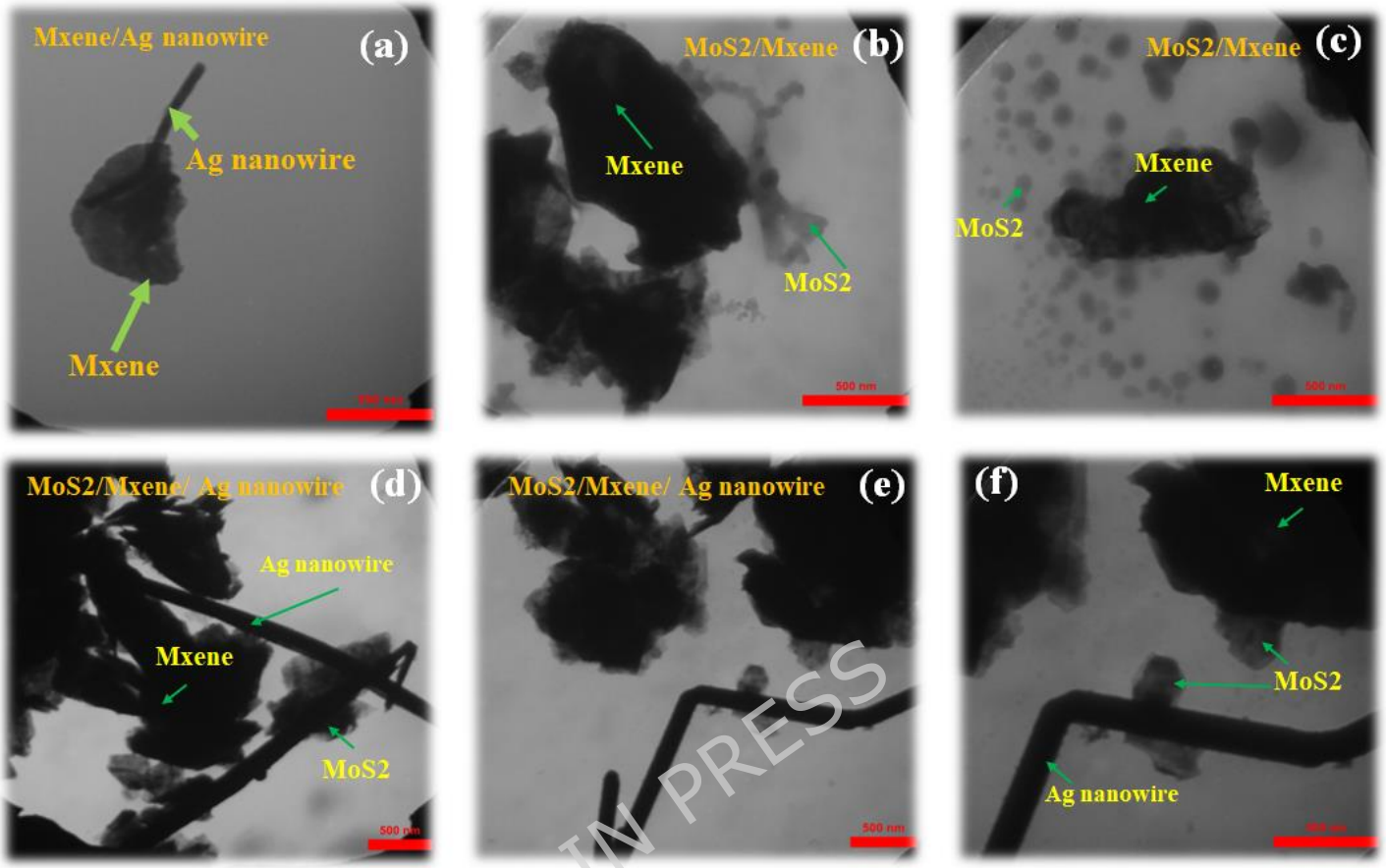

Fig.5. TEM images of (a) Ti_3C_2 MXene/Ag nanowires, (b,c) (Ti_3C_2 MXene/MoS_2), (d,e,f) (Ti_3C_2 MXene/ MoS_2/Ag nanowires)

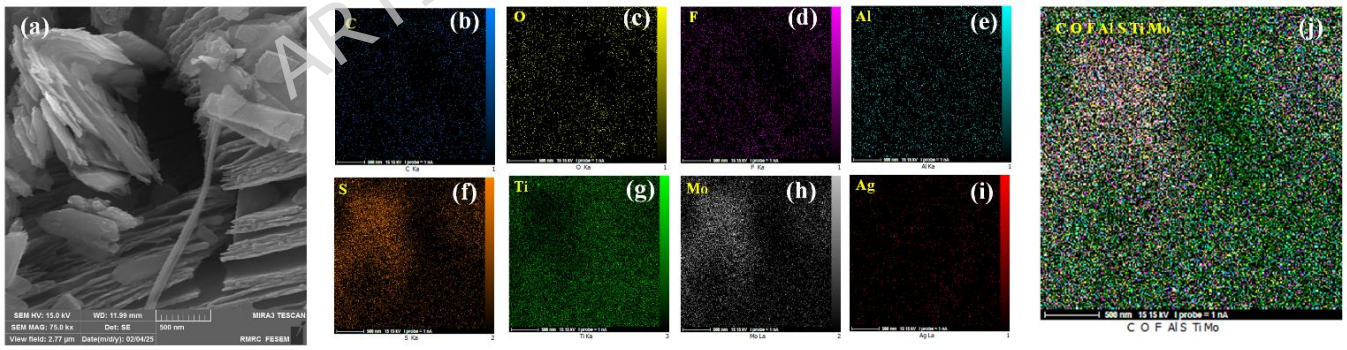

(k)

Elt	Line	Int	Error	K	Kr	W%	A%	ZAF	Formula	Ox%	Pk/Bg	Class	LConf	HConf	Cat#
C	Ka	40.8	5.4246	0.1267	0.0692	21.34	39.67	0.3243		0.00	29.53	A	20.39	22.30	0.00
O	Ka	29.1	5.4246	0.0450	0.0246	15.84	22.11	0.1551		0.00	10.83	A	15.00	16.68	0.00
F	Ka	42.0	5.4246	0.0452	0.0247	13.21	15.53	0.1870		0.00	11.25	A	12.63	13.79	0.00
Al	Ka	22.3	1.7473	0.0121	0.0066	0.97	0.81	0.6783		0.00	3.66	B	0.91	1.03	0.00
S	Ka	105.6	4.0658	0.0767	0.0419	4.55	3.17	0.9220		0.00	14.14	A	4.42	4.67	0.00
Ti	Ka	420.1	0.9634	0.5810	0.3174	36.48	17.00	0.8700		0.00	54.87	A	35.97	36.99	0.00
Mo	La	51.4	4.0658	0.0832	0.0454	5.55	1.29	0.8178		0.00	14.14	A	5.33	5.78	0.00
Ag	La	16.0	4.0658	0.0300	0.0164	2.05	0.42	0.8012		0.00	3.59	B	1.90	2.19	0.00
				1.0000	0.5462	100.00	100.00			0.00					0.00

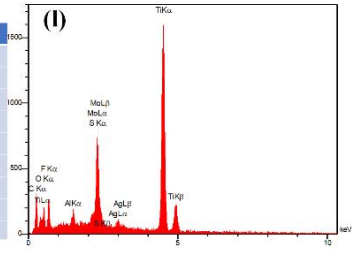

Fig. 6. Elemental distribution using EDS mapping and spectra of the fabricated material.

Figure 7a shows the Raman spectra of the synthesized materials. In the spectrum of pure Ti_3C_2 MXene, several peaks between 0 to 1000 cm^{-1} correspond to C-Ti vibration modes. The MoS_2 features prominent E^1_{2g} and A_{1g} peaks at 370 cm^{-1} and 410 cm^{-1}, respectively. The ratio of intensity of the A_{1g} to E^1_{2g} peaks offers key observations on the characteristics of the MoS_2 planes. For the Ti_3C_2 MXene/MoS_2/AgNWs composite, the presence of the characteristic E^1_{2g} and A_{1g} peaks confirms the successful deposition of MoS_2 and validates the fabrication of this film.

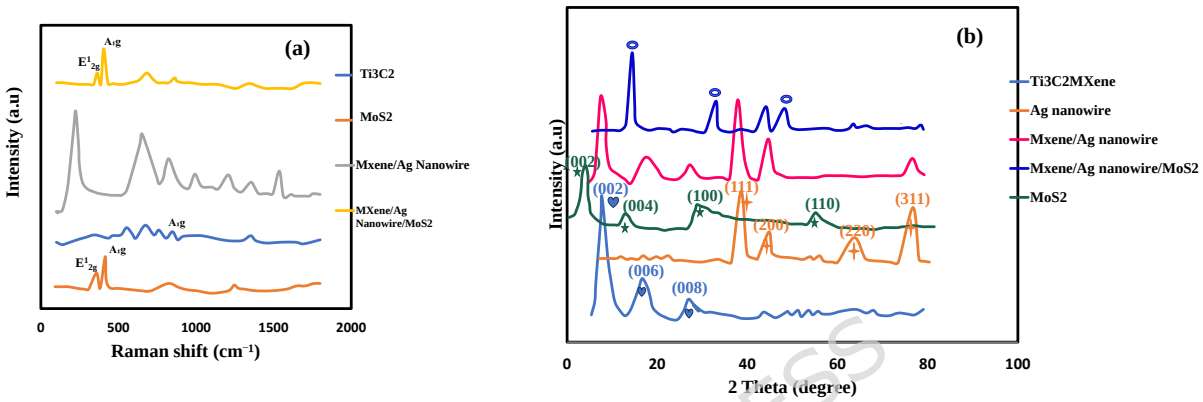

Fig 7. (a) RAMAN pattern, and **(b)** XRD pattern of material synthesized.

The XRD pattern in **Figure 7b** displays distinctive peaks at 7.0°, 17.3°, 27°, and 60.9°, which are associated with the (002), (006), (008), and (110) crystallographic planes of Ti_3C_2 MXene[26]. Notably, when integrated with Ag nanowires, the primary diffraction peak of Ti_3C_2 shifts to a lower angle, indicating an increased interlayer distance for the (002) plane. This likely results from the intercalation of Ag nanowires among the MXene sheets, causing lattice expansion. Additional diffraction peaks appear at 38.1°, 43°, 66°, and 77.8°, corresponding to the (111), (200), (220), and (311) planes of silver nanowires, confirming their presence within the composite structure. Diffraction peaks of MoS_2 appear at 9.2°,16.1°, 31°, and 57.8°, which are assigned to the (002), (004), (100), and (110) reflections, respectively[27]. The emergence of MoS_2-specific reflections at 17.6°, 34.0°, and 47.7° in the MXene/AgNW/MoS_2 construct confirms its MoS_2 integration, differentiating it from the MXene/AgNW baseline. The results of XRD shows the successful synthesis of the MXene/AgNW/MoS_2.

The AFM analyses of the prepared material (AgNWs/MoS_2/Ti_3C_2 MXene) including topography 2D, topography 3D and phase presented in **Figures 8(a-c)** show the texture and topographical features of its surface. The sharp peaks and troughs seen in the images reveal the specific arrangement and dimensions of the MoS_2, offering clues about its distribution. These features provide valuable information about the surface texture and the tendency for particles to cluster. Additionally, the Ti_3C_2 MXenes exhibit a smoother surface compared to MoS_2, showcases a layered configuration, where Ti_3C_2 MXene consists of flat, sheet-like layers **(Figure8 (a, b))**. Although the density of AgNWs is low, they effectively serve acting as bridges between the 2D islands, creating a cohesive and highly conductive framework that improves charge transfer across the entire system (**Figure8c)**. While AgNWs possess high intrinsic conductivity, the channel

in our device benefits from a moderately lower nanowire density to preserve gate tunability and avoid metallic shorting. The AgNWs form a conducting network that enables charge transport without dominating the semiconducting channel behavior, and the density is deliberately chosen to minimize shorting paths while still providing lateral conductivity.

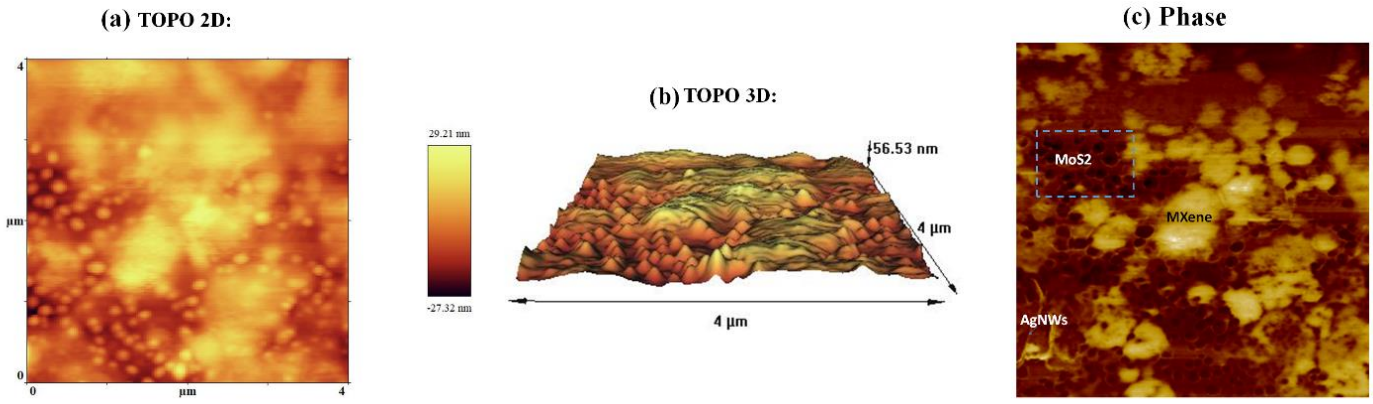

Fig8. AFM characterization of AgNWs/MoS_2/Ti_3C_2 MXene: (a) 2D topographical map, (b) 3D surface profile, and (c) phase image

Electrical characterization for three transistors array Without biomarkers

The electrical characterization of the proposed transistors with varying channel materials—(Ti_3C_2 MXene /Ag Nanowire), (MoS_2/Ti_3C_2 MXene), and (MoS_2/Ti_3C_2 MXene/AgNWs), (MoS_2/AgNWs)—were initially evaluated as individual transistors operating independently of glucose, as illustrated in **Figures 9(a-f).** This assessment includes the output mode transfer mode characteristic curves of the FETs.

First, the FET with a (Ti_3C_2 MXene /Ag Nanowire) channel was analyzed, as shown in **Figures 9(a,b)**. The output characteristic curve in **Figure 9a** indicates that the drain current (I_{ds}) for this FET-based sensor increases linearly with the V_{ds} from 0 to 3V, while the gate-source voltage (V_{gs}) varies from -1V to -4V, reflecting beneficial Ohmic response. Beyond V_{ds} = 3V, the device enters saturation, resulting in a constant I_{ds} despite increases in V_{ds}. The output characteristics shown in **Figure 9b** demonstrate that I_{ds} decreases with positive V_{gs} and increases with the V_{gs} values become more negative, it emphasizes a stronger gate influence over the FET channel. The estimated threshold voltage (Vt) is around -0.2V. as shown in **Figure 9b**.

Figures 9(c,d) illustrate the combination of Ti_3C_2 MXenes with MoS_2 (Ti_3C_2 MXenes/MoS_2), which harnesses the benefits of 2D materials. This combination structure leverages MoS_2's strong conductivity and Ti_3C_2 MXenes' tunable properties, leading to enhanced electron transport and improved overall FET performance. Their synergistic interaction boosts key electrical parameters like transconductance (g_m).

Furthermore, integrating Ag Nanowires into the Ti_3C_2 MXene/MoS_2 channel (AgNWs/ Ti_3C_2 MXene/MoS_2), as shown in **Figures 9(e,f),** further increases the FET's gm. The Ag Nanowires act as excellent conductors, strengthening channel conductivity. Their interaction with the hybrid matrix provides additional pathways for charge flow, resulting in superior transistor functionality and higher I_{ds}. Therefore, the transistor with the MoS_2/ Ti_3C_2 MXene/Ag NWs channel demonstrated the highest I_{ds} amplification and g_m among the tested devices.

The FET with a (MoS_2 /Ag Nanowire) channel was analyzed, as shown in **Figures 9(g,h)**. The output characteristic curve in **Figure 9g** indicates that the I_{ds} for this FET-based sensor increases linearly with the V_{ds} from 0 to 4V, while the V_{gs}) varies from 1V to 4V, reflecting beneficial Ohmic response. Beyond V_{ds} = 4V, the device enters saturation, resulting in a constant I_{ds} despite increases in V_{ds}. The output characteristics shown in **Figure 9h** demonstrate that I_{ds} increases with positive V_{gs}, it emphasizes a stronger gate influence over the FET channel. The estimated Vt is around 0.1V. as shown in **Figure 9h**.

Figure 9(i-p) show g_m and on-off ratio for different composite materials of the channel layer. Overall, the FET biosensor with an AgNWs/ Ti_3C_2MXene/MoS_2 channel demonstrates stronger g_m and on-off ratio compared to other transistors.

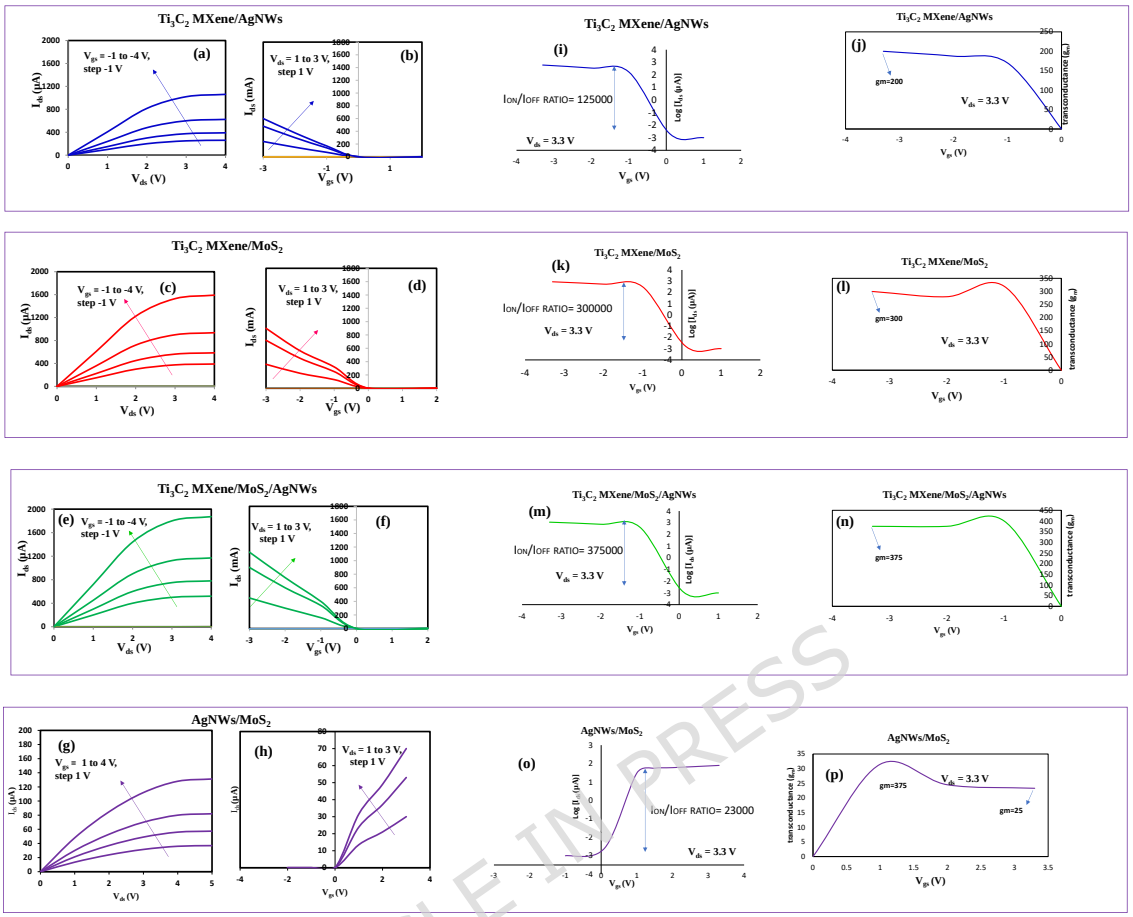

Fig9. The electrical properties of different transistors studied: (a,b) transistor made of Ti_3C_2 MXene combined with AgNWs, (c,d) transistor made of Ti_3C_2 MXene paired with MoS_2, and (e,f) transistor featuring channel of Ti_3C_2 MXene integrated with both AgNWs and MoS_2. (g,h) transistor made of AgNWs and MoS_2. (i-p) g_m and on-off ratio for different composite materials of the channel layer.

Electrical characterization for 3 FET Sensors array for Glucose Detection

We developed three FET sensor materials for glucose detection in sweat. **Figure 10a** shows the correlation between the I_{ds} and the V_{ds} at a glucose concentration of 0.1 µM across different channels of FET sensors. The results indicate that the AgNWs/Ti_3C_2 MXene/MoS_2 composite exhibits a higher I_{ds} compared to the other composites, prompting us to select this FET sensor for further analysis of glucose responses in sweat.

Figure 10b depicts how I_{ds} varies with glucose concentration at different V_{ds} (with the V_{gs} set to -3.3 V). The findings reveal that raising V_{ds} at a fixed V_{gs} boosts both I_{ds} and the sensor's sensitivity. Similarly, **Figure 10c** demonstrates the (I_{ds}- V_{gs}) curves for various glucose concentration at different V_{gs} (with V_{ds} fixed at 1 V), indicating that a higher V_{gs} also increases I_{ds} and sensitivity.

Figures 10(d-f) show the three linear range from 0 to 10 mM, achieving a sensitivity of 355 $mA \cdot mM^{-1}$, The FET exhibits a strong linear response, and a LOD of 0.001 µM.

The LOD is defined as the lowest concentration of an analyte that can be distinguished from background noise with a stated level of confidence. The LOD has been calculated using a representative blank dataset and a calibration slope[28]. A widely used practical estimate is:

$$\text{LOD} = \frac{3.3 \times S_{Dblank}}{m} \quad (1)$$

where S_{Dblank} is the standard deviation of the blank response and m*m* is the slope of the calibration curve in the same response units per concentration unit. The LOD's numeric value depends on the units of m and S_{Dblank}.

The sensor response has been measured for blank samples (no analyte) and obtained a series of responses: Responses (unit: µA): 1680, 1680.2, 1680.1, 1680.2, 1680 (unit: µA)

The sensor response has been converted to a standard deviation according to equation (2):

$$S = \sqrt{\frac{1}{n-1}\sum_{i-1}^{n}((x_i - x)^2} \approx 0.14 \text{ (unit: µA)} \quad (2)$$

The calibration slope is m=355.56 µA/µM, determined from the calibration curve in **Figure10d**. Finally, LOD can be calculated according to:

$$\text{LOD} = \frac{3.3 \times S_{Dblank}}{m} = \frac{3.3 * 0.14}{356} = 0.001 \text{ µM} \quad (3)$$

Overall, the glucose FET biosensor with an AgNWs/ Ti_3C_2MXene/MoS_2 channel demonstrates stronger sensitivity and a lower detectable concentration compared to other transistors.

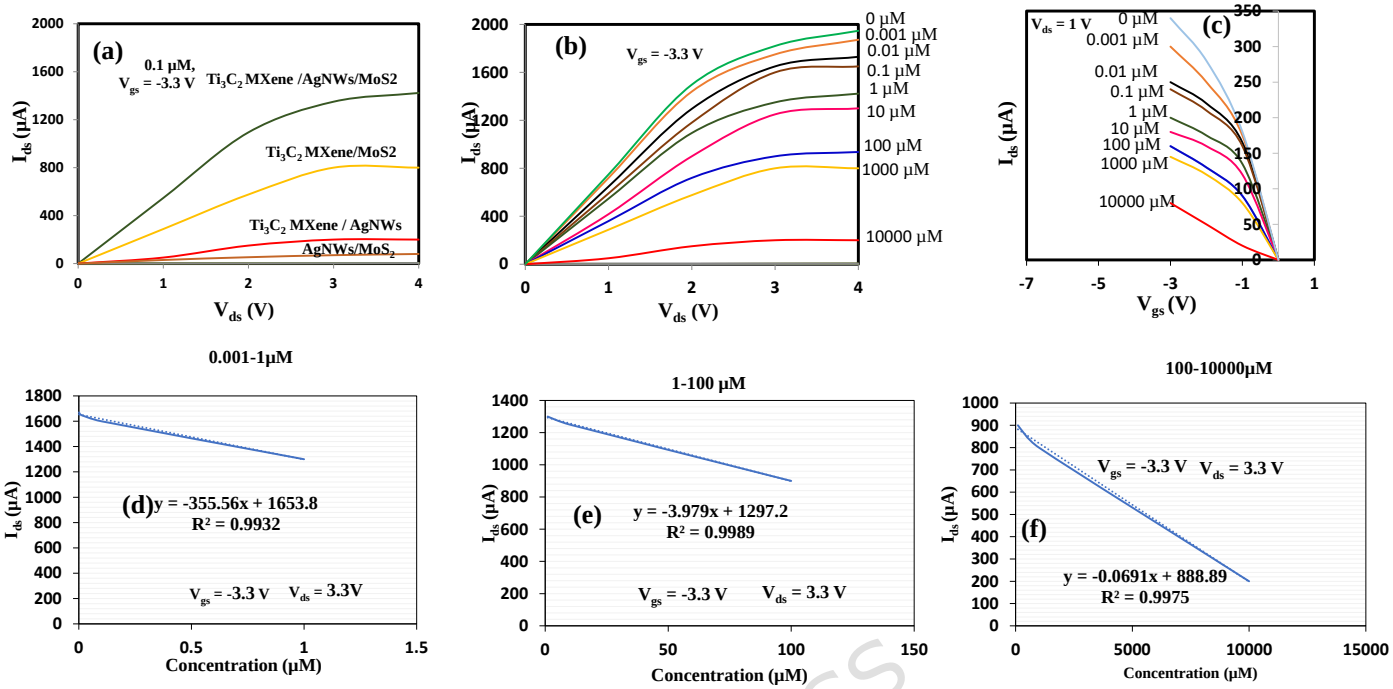

Fig. 10. The electrical response towards glucose: (a) A comparison of transistors with different channels. (b, c) The electrical characteristics of the transistor, including (I_{ds}–V_{ds}) and (I_{ds}–V_{gs}) curves, using a Ti_3C_2 MXene/AgNWs/MoS_2 channel, respectively (d) Calibration plot for the transistor featuring a Ti_3C_2 MXene/AgNWs/MoS_2 channel.

Electrical characterization of the Dual-Mode FET sensor array for pH Fluctuations

The Ti_3C_2 MXene and MoS_2 acts as a dual-mode material that interacts to pH changes. Therefore, AgNWs/Ti_3C_2 MXene/MoS_2 nanocomposite functions as a dual-mode FET for detecting pH fluctuations. According to **Figure11 a**, the calibration curve (I_{ds} as a function of pH level) exhibits a strong linear response on the pH in the range from 3 to 9, with an R^2 value of 0.9971.

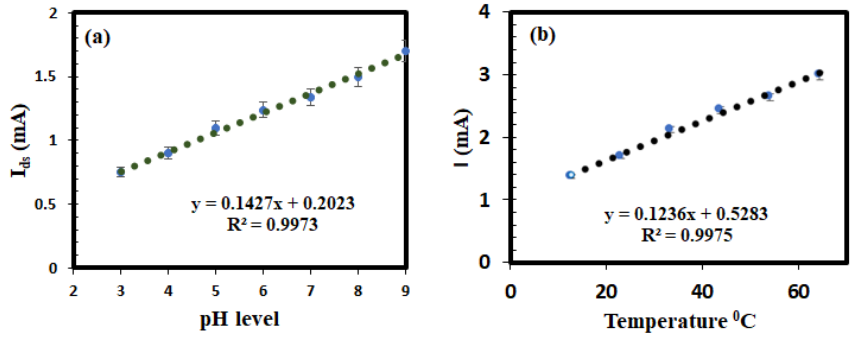

Fig11 The calibration characterization (a) for pH transistor with channel of Ti_3C_2 MXene/AgNWs /MoS_2, and (b) for rGO/PEDOT:PSS temperature sensor.

Design and Characterization of rGO/PEDOT:PSS Temperature Sensor

To ensure accurate glucose measurements, temperature sensors should be incorporated for proper calibration, as temperature fluctuations can lead to inaccuracies. By placing a temperature sensor close to the glucose sensors, we can accurately monitor temperature changes in the vicinity.

For calibration of the proposed temperature sensor, we positioned temperature sensor on a heater alongside a commercial temperature sensor, gradually rising the temperature from 17 °C to 64 °C while recording the electrical characteristics (I-V) of the sensor. The proposed temperature sensor is calibrated using the values from the commercial temperature sensor. We observed a linear correlation between the current changes and temperature corresponding to the physiologically normal range of 17 °C to 64 °C, with an R^2 value of 0.9973 **(Figure11b).**

The Sensing Mechanism of glucose and pH biosensors and performance of Microfluidic Channel

The microfluidic layers are composed of PDMS and feature coil-shaped microfluidic channels, along with inlet and outlet wells for self-driven sweat capture. The laser settings were optimized to achieve the desired channel dimensions, specifically a depth of 20 µm and a width of 250 µm, while considering the thickness of the PDMS, which facilitated the formation of the coil-shaped microfluidic channels. The design of the microfluidic channels ensures that sweat flows directly over the intended pH and glucose FETs, preventing contact with the temperature sensor within the device. Additionally, the temperature sensor is isolated from the glucose-sensing area by a layer of PDMS, effectively preventing cross-contamination.

Ti_3C_2 MXene provides a highly conductive, two-dimensional surface with abundant terminal groups that can facilitate chemical interfacing and rapid charge transfer[12]. MoS_2 contributes favorable catalytic sites and a tunable band structure that enhances electrochemical oxidation processes relevant to glucose sensing[29]. AgNWs form a percolating network that accelerates electron transport from the sensing interface to the electrode, improving signal transduction and response time[30].

A composite of Ti_3C_2 MXene, MoS_2, and AgNWs was employed for selective glucose detection. Incorporating MoS_2 into the Ti_3C_2 MXene sensing channel promotes glucose oxidation, generating free electrons. The AgNWs, known for their excellent electrical conductivity, accelerate the movement of electrons to the Ti_3C_2 MXene, which then relays them efficiently to the copper electrodes.

For pH monitoring, both MoS_2 and Ti_3C_2 MXene exhibit strong interactions with hydrogen ions (H^+). This interaction increases electrical current of the p-type FET sensor in response to rising H^+ concentration, thereby enhancing its sensitivity to changes in pH.

Repeatability, Stability, Reproducibility, and Selectivity Tests

To assess repeatability, a single biosensor was tested three times consecutively at a glucose concentration of 100 µM. The resulting relative standard deviation (RSD) was just 0.013%, demonstrating exceptional measurement consistency **(Figure 12a).** Reproducibility was further validated by testing ten independently fabricated biosensors under the same conditions, also yielding an RSD of 0.013%, confirming the high fabrication reliability and uniform performance across devices **(Figure 12b).**

The long-term stability of the biosensor was evaluated over a three-week period. The sensor retained 98.3% of its initial response, indicating excellent durability **(Figure 12c).** Selectivity testing involved exposing the sensor to a mixture containing 100 µM glucose and a concentration of 6 mM for various potential interfering substances, including K^+, uric acid, Na^+, ascorbic acid, dopamine, Cl^-, lactose, and fructose. The sensor exhibited a robust response to glucose with negligible interference from these compounds, underscoring its high selectivity **(Figure 12d).**

The influence of environmental humidity on sensor performance was examined by adjusting relative humidity (RH) levels between 22% and 90% **(Figure 12e).** The sensor consistently maintained stable operation across the tested range. Even following storage in high-temperature and high-humidity for two hours, the device continued to function reliably, demonstrating its robustness under varying environmental stresses.

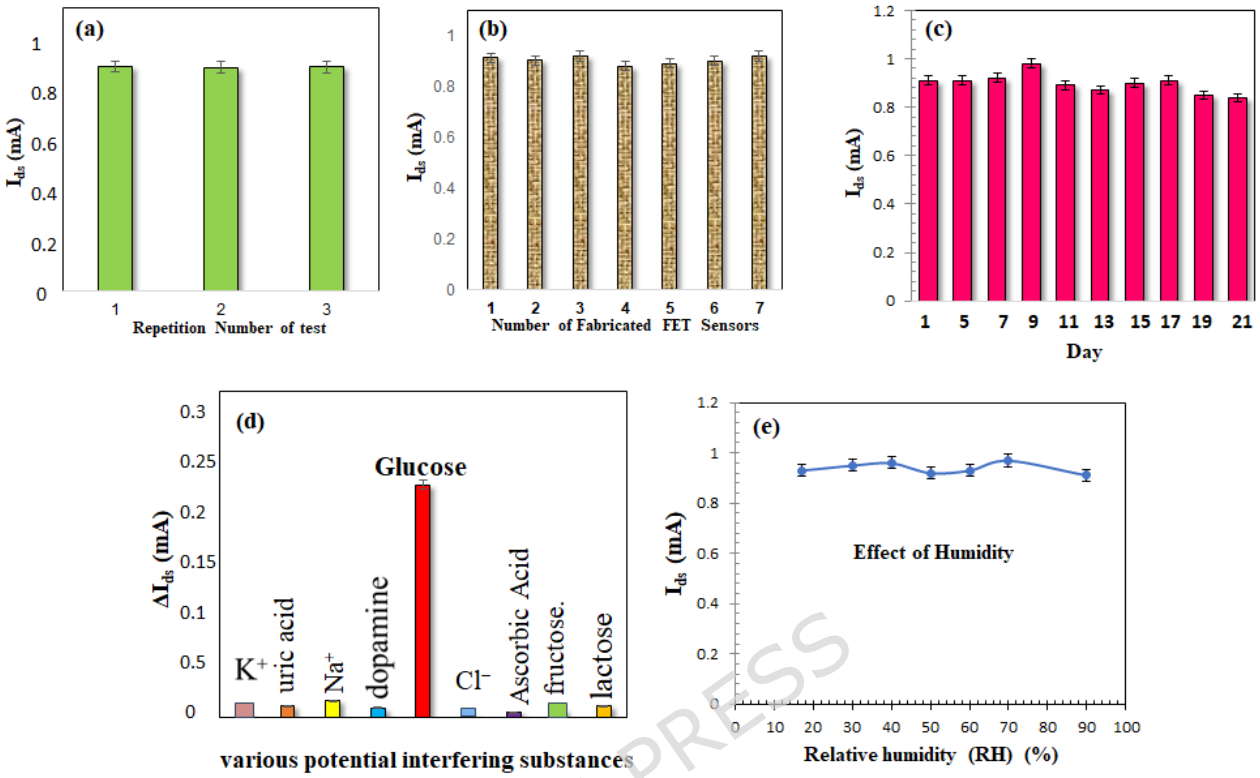

Fig. 12. Evaluations of (a) repeatability, (b) reproducibility, (c) stability, and (d) selectivity for various added interferences, (f) influence of humidity on the FET response towards 100 µM glucose.

Calibration of the FETs with Simultaneously Measured pH and Temperature

The glucose sensor boasts an impressive response time of just 1 second, facilitating quick in vitro analysis of its calibration curves for glucose concentrations ranging from 0.001 µM to 10 mM, across different pH concentrations and temperatures. To calibrate the sensor, its responses to temperature and pH changes are assessed through simultaneous measurements. The I_{ds} increases with both temperature and pH at specific glucose concentrations. Correction factors (slope and intercept) are then calculated for the linear relationship between current and glucose concentration, taking into account body temperature **(Figure 13a)** and sweat pH **(Figure 13b).** The final glucose concentration is calculated using the adjusted slope and intercept obtained from the linear fit.

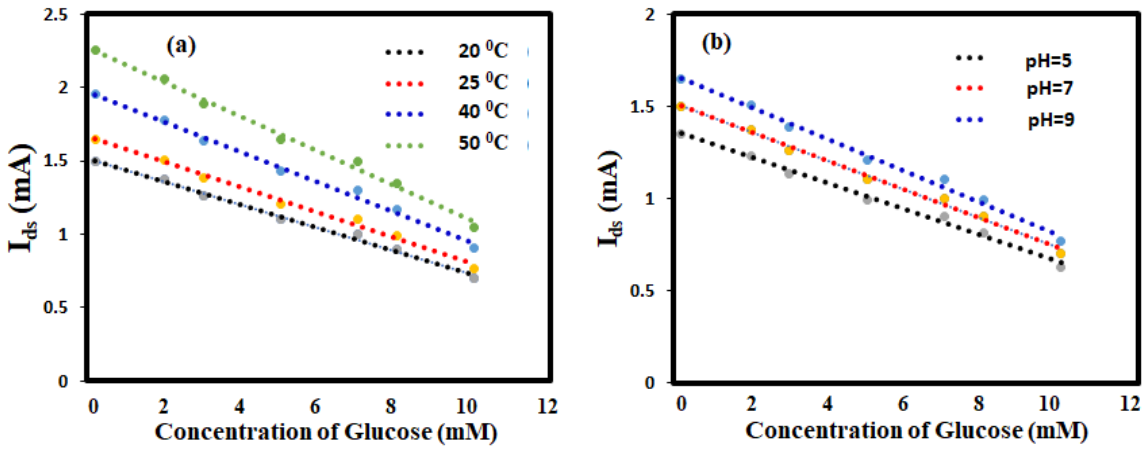

Figure 13. (a) The calibration plots for the glucose FET sensor under various conditions. (a) temperatures variation, and (b) pH different levels.

The accurate determination of glucose concentration, based on measured current, is calibrated relative to observed changes in pH and temperature. According to **Figure 13**, the linear fit of the glucose biosensor shows the relationship between the I_{ds} of FET and glucose concentration (g) at a pH of 7 and a temperature of 24°C:

$$I_{ds} = -S_{ref}\, g + I_{ref} \quad (1)$$

where the slope S_{ref} (mA/mM^{-1}) represents the sensitivity and I_{ref} is the intercept.

The sensor's response to glucose concentration can be adjusted for the effects of temperature and pH by using compensation factors S_{temp} and I_{temp} for temperature, and S_{pH} and I_{pH} for pH. These compensation factors are defined as the ratio of the measured values to the reference values (pH = 7 and room temperature).

The variation factors for each parameter are shown as follows:

$$S_{temp} = \frac{Slope\ \ as\ a\ function\ \ of\ \ \ Temp}{S_{ref}} \quad (2),$$

$$I_{temp} = \frac{Intercept\ as\ a\ function\ \ of\ \ \ Temp}{I_{ref}} \quad (3),$$

$$S_{pH} = \frac{Slope\ \ as\ a\ function\ of\ \ \ pH}{S_{ref}} \quad (4), \text{ and}$$

$$I_{pH} = \frac{Intercept\ as\ a\ function\ of\ \ \ pH}{I_{ref}} \quad (5)$$

Finally, the I_{ds} as a function of glucose concentrations after temperature and pH calibration is:

$$I_{ds(temp,pH)} = -S \times g + I = -S_{ref} \times S_{pH} \times S_{temp} \times g + I_{ref} \times I_{pH} \times I_{temp} \quad (6)$$

Human Sweat Sample Tests

A correlation exists between blood glucose and sweat glucose levels in real human samples, as illustrated in **Figure 14.** This relationship is essential because it suggests that glucose concentrations in sweat can serve as a reliable indicator of blood glucose levels. In continue, fasting blood samples were collected from participants after obtaining informed written consent from each individual. The glucose levels measured by the proposed smartwatch-integrated biosensor were then compared to those obtained using a standard commercial glucometer, as presented in **Table 1**. The close correlation between the two sets of results validates the accuracy of the developed FET-based sensor. These findings support the sensor's capability for reliable glucose detection not only in blood but also in human sweat.

Table1: Result obtained by the proposed smart watch are compared with those measured from a commercial glucometer. Glucose unit is mg/dl.

Participant ID	Age	Glucose measurement from the glucometer	Glucose measurement from the smart watch	**Participant ID**	Age	Glucose measurement from the glucometer	Glucose measurement from the smart watch
1	16	70	74	**11**	25	74	76.5
2	22	82	85.5	**12**	48	121	117
3	24	73	75.5	**13**	55	148	145.5
4	30	75	73	**14**	57	111	109
5	17	80	78.5	**15**	68	99	98
6	43	84	81	**16**	73	150	146
7	50	98	94.5	**17**	14	78	81
8	26	90	88	**18**	81	107	111.5
9	32	76	73.5	**19**	24	89	93
10	27	103	101.5	**20**	66	83	80.5

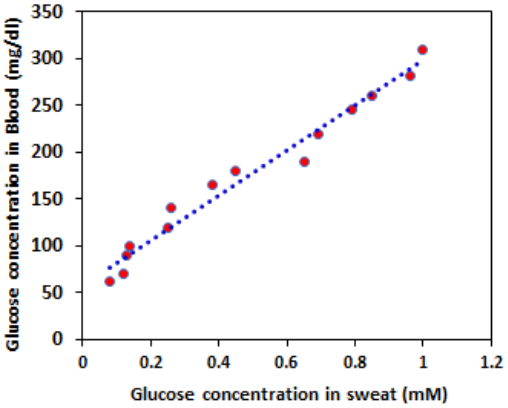

Fig14. The relationship between glucose in blood and sweat in human samples.

Table 2 presents a comparison with recently reported wearable sweat glucose sensors. The developed sensor outperforms existing technologies with its wide detection range (0–10 mM), an ultra-low detectable concentration of 0.001 µM, a strong sensitivity of 355 $mA \cdot mM^{-1}$, establishing a new benchmark in wearable biosensor performance.

Table 2. Recently published studies on wearable sensors for measuring sweat glucose levels.

Material	Recognition method	Sensitivity µA mM^{-1}	DR mM	LOD (µM)	Ref
Gold-ZnO	Glucose Oxidase	-	0.047-0.305	5.5	[31]
PB/MWCNT-Fe_3O_4	Glucose Oxidase	-	0.01–0.2	0.31	[32]
Ti_3C_2 MXene/Platinum	Non-Enzymatic	3.43	0-8	-	[12]
PEDOT:PSS/ MXene	Glucose Oxidase	-	0.05-1.30	32	[26]
ZnFe(PBA)/$Ti_3C_2T_x$	Glucose Oxidase	973.42	0.01-1	3.036	[28]
Gold	Glucose Oxidase	0.002	0-0.3	-	[33]
Fe/PHEMA/Cu hydrogel	Non-Enzymatic	66.06	0–4	9.99	[34]
AgNWs/ Ti_3C_2 MXene /MoS_2	Non-Enzymatic	355000	0-10	0.001	Our work

Conclusion

In summary, this paper marks the glucose monitoring without piercing the skin through the development of a high-performance wearable FET biosensor. By integrating this sensor into a smartwatch platform with Internet of Things (IoT) capabilities, real-time glucose tracking becomes seamless and easy to use, offering a promising alternative to traditional glucometers. The sensor's architecture leverages a ternary composite channel composed of MoS_2, Ti_3C_2 MXene, and silver nanowires. Each component contributes distinct advantages: silver nanowires enhance electrical conductivity and mechanical stability; MoS_2 boosts electrochemical response; and Ti_3C_2 MXene provides tunable surface functionality and excellent charge transport properties. Together, they enable exceptional sensor performance, including high sensitivity (355 mA mM^{-1}), a broad linear detection range (0.001 µM to 10 mM), a remarkably low LOD (0.001 µM), excellent repeatability, minimal cross-interference, and strong long-term stability. Overall, the integration of this advanced FET glucose biosensor into a wearable smartwatch platform demonstrates its practical viability for non-invasive glucose monitoring. It offers an accessible, accurate, and efficient tool for managing glucose levels through sweat analysis, representing a major leap forward in personal health monitoring technologies.

Methods

Material.

The materials utilized in this study were sourced from Sigma-Aldrich, ensuring high purity essential for precise experimental outcomes. Among these materials were ethanol, with a purity of 96%; D (+) glucose, which had a purity of 97%; Nafion, a sulfonated tetrafluoroethylene-based fluoropolymer membrane; polydimethylsiloxane (PDMS), a silicon-based elastomer; thiourea; ammonium molybdate; PEDOT:PSS, a conductive polymer mixture; N,N-dimethylformamide (DMF); reduced graphene oxide (rGO); lithium fluoride (LiF); phosphate-buffered saline (PBS), a buffer solution maintaining pH stability; hydrochloric acid (HCl) solution; Ti_3AlC_2, a member of the MAX phase ceramics; and sodium hydroxide (NaOH).For the fabrication of the biosensor's sensitive layer, a specific preparation protocol was followed. Nafion was diluted with ethanol to produce a 5% solution, achieved by mixing equal weights (1:1 wt%) of Nafion and 96% ethanol. The mixture was then subjected to vigorous agitation for one minute to ensure homogeneous dispersion. This Nafion-ethanol solution was subsequently used as the conductive polymer matrix to facilitate effective immobilization of sensing elements and enhance electrochemical performance of the biosensor. The phosphate-buffered saline used was 0.01 M in concentration with a pH value of 7.4.

Characterization

For characterization, the products were analyzed through various techniques: XRD (BRUKER D8 Advanced) and FE-SEM using a Carl Zeiss AURIGA Crossbeam device for structural and morphological assessment. Raman spectra were obtained using a Renishaw in Via system, and

atomic force microscopy (AFM) imaging was performed with an ARA AFM device. Electrical measurements of the FETs, including current recordings, were carried out using a Keithley instrument (2450), along with voltages provided by a GPS power supply.

Synthesis of Ti_3C_2 MXene

Employing the on-site hydrofluoric acid etching approach, Ti_3C_2 MXene was created. Initially, 1.2 gram of LiF was added little by little to 25 ml of 9 M hydrochloric acid solution, and the mixture was constantly agitated for 25 minutes, allowing the LiF to fully dissolve. After carefully adding 1 g of Ti_3AlC_2 to the LiF/HCl combination, mixture was agitated for 12 hours while maintained in an ice bath. Following the etching procedure, the powder that resulted was gathered through the process of centrifuging and extensively cleaned with DI water until the pH of the liquid was 6. For ten hours, the finished Ti_3C_2 powder was vacuum-dried at 50 °C. Aluminum is successfully extracted from the Ti_3AlC_2 precursor using this synthesis technique, resulting in Ti_3C_2 MXene.

Synthesis of Silver Nanowires (AgNWs)

AgNWs were synthesized using silver chloride (AgCl), following established procedures. In summary, an aqueous solution of silver nitrate ($AgNO_3$) (0.5 M, 10 mL) was combined with an aqueous sodium chloride (NaCl) solution (1.0 M, 10 mL) while continuously stirred continuously at 1000 rpm in darkness for a duration of 5 minutes. The resulting AgCl precipitate was filtered, washed with ultrapure water, and vacuum-dried. For the synthesis of AgNW, 300 mg of polyvinylpyrrolidone (PVP) was dissolved in 20 mL of ethylene glycol. This mixture was stirred at 1500 rpm and heated to 160 °C for 15 minutes. Afterward, 20 mg of AgCl was added to the solution. Following an additional 10 minutes of stirring, 100 mg of $AgNO_3$ was introduced, and the mixture was stirred at 1500 rpm while maintaining a temperature of 160 °C for 25 minutes.

Synthesis of MoS_2 deposited on Ti_3C_2 MXene

To prepare the combination, 1 gram of pre-prepared Ti_3C_2 MXene was first dissolved in a mixture of 50 mL of DI water and an equal volume of DMF. The solution was subsequently treated with ultrasonication to ensure a uniform dispersion. A total of 1.5 grams of ammonium molybdate and 3 grams of thiourea were slowly introduced into the solution while stirring continuously for thorough integration. The resulting solution was transferred into a 100 mL Teflon-lined autoclave, which was then securely sealed, and subjected to heating at 175 °C for 19 hours. After the reaction process, the autoclave was left to cool naturally to room temperature. The product was then recovered via centrifugation, rinsed repeatedly with DI water and ethanol to eliminate residual impurities, and finally dried by oven heating at 60 °C for a duration of 8 hours. The obtained material was designated as MoS_2 catalyst supported on Ti_3C_2 MXene.

Synthesis of Ti_3C_2 MXene/AgNWs

To synthesize Ti_3C_2 MXene/AgNW, 1 gram of pre-prepared Ti_3C_2 MXene was combined with 5 mg of pre-prepared AgNWs in 50 mL of deionized water. The combination was subsequently ultrasonicated to ensure a uniform dispersion. The final material was collected via centrifugation and dried by oven heating set to 60 °C for a duration of 8 hours. The obtained substance was designated as Ti_3C_2 MXene/AgNW.

Synthesis of Ag Nanowire Cross-Linked MoS_2 Nano-Flakes and Ti_3C_2 MXene Nano-Sheets (MoS_2-Ti_3C_2 MXene/AgNW)

To synthesize the MoS_2-Ti_3C_2 MXene/AgNW, 1 g of synthesized powder of MoS_2 deposited on Ti_3C_2 MXene (MoS_2-Ti_3C_2 MXene) was mixed with 5mg of pre-prepared AgNW in 50 mL of deionized water. The blend underwent ultrasonication to form a uniform suspension. The final material was collected via centrifugation, and dried by oven heating at 60 °C for 6 hours. The resulting composite was designated MoS_2-Ti_3C_2 MXene/AgNW.

Figure 1(a-d) shows the schematic diagram depicting the fabrication process of the FET sensors channel for AgNWs, Ti_3C_2 MXene/MoS_2, Ti_3C_2 MXene/AgNW, and AgNWs/MoS_2/ Ti_3C_2 MXene, respectively.

Design and manufacturing FET electrodes array

Copper electrode arrays on a plastic substrate were manufactured using a lithography technique. The mask pattern (source and drain interdigitated electrodes) was drawn with AutoCAD software, specifying an electrode thickness of 200 µm and a gap of 150 µm between the electrodes. The fabrication process commenced with the cleaning and treatment of the flexible substrate to ensure proper adhesion. Subsequently, a layer of S1813 photoresist was applied and spin-coated at 5000 rpm for 1 minute to achieve a uniform thickness. The photoresist was exposed to ultraviolet light for 30 seconds through the mask, which defined the desired patterns. Following exposure, the photoresist was developed to reveal the underlying substrate areas designated for copper deposition. A copper layer with a thickness of 300 nm was then deposited onto the substrate using a sputtering technique. After the deposition process, the remaining photoresist was stripped away, resulting in a thin copper layer that formed the desired pattern on the flexible substrate **(Figure 2(a-d)).** The designed flexible transistor array includes six FETs; three FETs (T1, T3, T5) are positioned on the left side of the substrate with a common side gate, while the remaining three FETs (T1, T3, T5) are positioned on the right side, also sharing a common side gate. The side gates are situated centrally, located between the source and drain electrodes, thereby facilitating transistor control.

Design and Fabrication of microfluidic channel

The smartwatch consists of three key parts: FET sensor array for measuring biomarkers, and a flexible microfluidic channel for sweat collection. The microfluidic layers are constructed from polydimethylsiloxane (PDMS), incorporating coil-shaped channels and inlet/outlet wells to facilitate self-driven sweat capture. The glucose and pH sensors are strategically positioned adjacent to the coil-shaped channels, while the temperature sensor is located nearby. To fabricate the microfluidic channels, a mixture of PDMS base and curing agent in a 10:1 ratio was thoroughly combined. and applied to an acetate sheet. The mixture was then cured at 70°C for 3 hours until fully solidified. The design layout of the microfluidic channels was created using Corel software, and a CO_2 laser system was employed to engrave the channel patterns. Laser parameters were optimized to achieve the desired depth and width of the channels based on the PDMS thickness, resulting in the formation of the coil-shaped microfluidic channels, as illustrated in **Figure 2e.**

Fabrication of glucose and pH FET Biosensors

The construction of wearable sensors begins with brush-scrubbing the electrodes in an aqueous solution, followed by ultrasonic cleaning in an aqueous bath to remove contaminants. To further improve cleanliness, the electrodes are rinsed with ethanol and acetone. An argon gas treatment is then applied to ensure optimal surface purity. Next, 15 µL (2 mg/mL) of every synthesized solution— Ti_3C_2 MXene/AgNW, MoS_2/Ti_3C_2 MXene, AgNWs/MoS_2 and MoS_2/ Ti_3C_2 MXene/AgNWs—is individually applied to the electrode array, creating distinct channels for glucose and pH wearable FET biosensors. After applying the composite layers, a protective channel layer of 1 µL Nafion is spread over the sensor surfaces. This careful process successfully fabricates three unique wearable FET sensors. Finally, the results from the three fabricated sensors are compared and discussed. The deposition is carried out using a spin coating technique at 3000 rpm for 30 seconds. Also, the sheet resistance has been measured for each channel composition that represent the mean performance of multiple sensors: the sheet resistance for silver nanowires/Ti_3C_2 MXene is 2.45 kΩ/Square, for Ti_3C_2 MXene/MoS_2 is 1.63 kΩ/Square, for MoS_2/Ti_3C_2 MXene/silver nanowires is 1.38 kΩ/ Square, and for MoS_2/silver nanowires is 23.5 kΩ/ Square.

Fabrication of temperatures sensor

A temperature sensor was fabricated using rGO/PEDOT:PSS ink (10mg/ml) through a stamp method on plastic substrate. A patterned stamp was created from a silicone elastomer, allowing for precise application of the ink. The ink was transferred onto the stamp and subsequently pressed onto the plastic substrate, followed by curing at room temperature to enhance electrical conductivity and adhesion.

Design and Fabrication of Smart Watch

Designing and fabricating a smart watch involves integrating a sensor array with FETs to monitor various physiological parameters such as glucose and temperature. The FETs serve as sensitive transducers that convert analog signals from these sensors into electrical signals for processing. To amplify these signals, an AD620 integrated circuit operational amplifier is employed, ensuring high precision and low noise. The watch's microcontroller, specifically the ESP32, plays a crucial role in managing sensor data, controlling the watch's functions, and offering connectivity through Bluetooth to mobile devices for real-time data syncing and notifications. Additionally, a compact LED display provides a user-friendly interface, enabling seamless interaction with the watch's features. This combination of components allows for a versatile and efficient smart watch design that caters to health monitoring and connectivity needs**.**

Figure3a shows the FET sensors Connections, Amplification of signals, Data processing, and OLED Display.

Figure3b shows electrical circuit of Voltage Regulator and Negative Voltage converter**.** Voltage Regulator ensures that the voltage supplied to the FET sensors and other parts of the circuit remains stable and within the necessary range for optimal operation, despite variations in input voltage or load conditions. The Negative Voltage Converter provides a negative gate voltage for FETs. This converter produces the negative voltage needed for optimal p-type FET performance, ensuring it functions as intended.

Figure3c shows Battery charger and Voltage Booster. The smartwatch utilizes a 3.7V lithium-ion, which is used for its rechargeability. The charger is designed to take in a standard 5V input, which is a voltage supplied by mobile USB chargers. The voltage booster steps up the output voltage from the 3.7V battery to the necessary 5V required by the ESP32 microcontroller chip. By using a voltage booster, the smartwatch can maintain the performance of the ESP32.

Human subjects

All ethical and experimental protocols were approved by the Health Research Center of Shiraz University of Technology (HRC of SUT) and carried out in accordance with relevant guidelines and regulations. For human subjects, informed consent was obtained from all participants.

Data availability

Data can be obtained by contacting the corresponding author upon request.

References

1 Acharya, R. *et al.* Single-Walled Carbon Nanotube-Based Optical Nano/Biosensors for Biomedical Applications: Role in Bioimaging, Disease Diagnosis, and Biomarkers Detection. *Advanced Materials Technologies*, 2400279 (2024).

2 Arthanari, S. *et al.* Fabrication of Porous Non-Enzymatic Glucose Sensing Electrodes Through Nanosecond-Laser Patterning of Metal–Organic Frameworks. *Advanced Materials Technologies* **9**, 2301561 (2024).

3 Deng, Y. *et al.* Stretchable liquid metal based biomedical devices. *npj Flexible Electronics* **8**, 12, doi:10.1038/s41528-024-00298-z (2024).

4 Farahmandpour, M., Haghshenas, H. & Kordrostami, Z. Blood glucose sensing by back gated transistor strips sensitized by CuO hollow spheres and rGO. *Scientific Reports* **12**, 21872 (2022).

5 Han, W. *et al.* A self-powered wearable noninvasive electronic-skin for perspiration analysis based on piezo-biosensing unit matrix of enzyme/ZnO nanoarrays. *ACS applied materials & interfaces* **9**, 29526-29537 (2017).

6 He, L. *et al.* A novel self-powered sensor based on Ni (OH) 2/Fe2O3 photoanode for glucose detection by converting solar energy into electricity. *Journal of Alloys and Compounds* **907**, 164132 (2022).

7 Hu, Y. *et al.* MXene-based flexible electronic materials for wound infection detection and treatment. *npj Flexible Electronics* **8**, 30, doi:10.1038/s41528-024-00312-4 (2024).

8 Farahmandpour, M., Dideban, D., Dehbali, M. M. & Kordrostami, Z. Smart Bioelectronics Glucometer with CNT/MXene-FET Test Strip Decorated with Silver NWs Featuring Alarm Functionality. *Sensors and Actuators A: Physical*, 117486 (2026).

9 Farahmandpour, M., Dideban, D., Dehbali, M. M. & Kordrostami, Z. Disposable Wireless FET Paper Sensor based on MWCNT/MXene/MoS2 Composite for Non-Invasive Glucose Detection in Saliva. *Journal of Alloys and Compounds*, 178715 (2025).

10 Kumar, R. & Singh, L. Ti3C2Tx MXene as electrocatalyst for designing robust glucose biosensors. *Advanced Materials Technologies* **7**, 2200151 (2022).

11 Li, M. *et al.* Three-dimensional porous MXene/NiCo-LDH composite for high performance non-enzymatic glucose sensor. *Applied Surface Science* **495**, 143554 (2019).

12 Li, Q.-F., Chen, X., Wang, H., Liu, M. & Peng, H.-L. Pt/MXene-Based Flexible Wearable Non-Enzymatic Electrochemical Sensor for Continuous Glucose Detection in Sweat. *ACS Applied Materials & Interfaces* **15**, 13290-13298, doi:10.1021/acsami.2c20543 (2023).

13 Farahmandpour, M., Kordrostami, Z., Rajabzadeh, M. & Khalifeh, R. Flexible bio-electronic hybrid metal-oxide channel FET as a glucose sensor. *IEEE Transactions on NanoBioscience* (2023).

14 Farahmandpour, M., Ansari, H. R. & Kordrostami, Z. Flexible Enzyme-Free Gate Engineered Bio-FET Glucose Sensor based on Nickel-Tungstate Microcrystals. *IEEE Sensors Journal* (2024).

15 Wang, B. *et al.* Wearable aptamer-field-effect transistor sensing system for noninvasive cortisol monitoring. *Science Advances* **8**, eabk0967, doi:doi:10.1126/sciadv.abk0967 (2022).

16 Zhao, C. *et al.* Implantable aptamer–field-effect transistor neuroprobes for in vivo neurotransmitter monitoring. *Science Advances* **7**, eabj7422, doi:doi:10.1126/sciadv.abj7422 (2021).

17 Farahmandpour, M. & Kordrostami, Z. Wearable MXene-enhanced organic Bio-FET paper patch for glucose detection in sweat with pH and temperature calibration. *Scientific Reports* **15**, 1-18 (2025).

18 Farahmandpour, M., Kordrostami, Z. & Haghshenas, H. Side-Gate-FET Test Strips for Invasive and Non-Invasive Saliva Based Glucose Monitoring Using GO-Catalyzed CuO-ZnO Hollow Spheres. *IEEE Sensors Journal* (2025).

19 Monfared Dehbali, M., Farahmandpour, M., Hamedi, S. & Kordrostami, Z. Development of a portable smart Glucometer with two electrode bio-electronic test strip patch based on Cu/Au/rGO/PEDOT: PSS. *Scientific Reports* **13**, 9505 (2023).

20 Xu, Y. *et al.* Pencil–paper on-skin electronics. *Proceedings of the National Academy of Sciences* **117**, 18292-18301, doi:doi:10.1073/pnas.2008422117 (2020).

21 Zhang, F. *et al.* Multi-modal strain and temperature sensor by hybridizing reduced graphene oxide and PEDOT: PSS. *Composites Science and Technology* **187**, 107959 (2020).

22 Farahmandpour, M., Sadeghfar, F., Asfaram, A., Ghaedi, M. & Javadian, H. Improving the sensitivity and detection speed of methane gas at room temperature using a nanosensor based on lead sulfide (PbS) colloidal quantum dots. *Results in Chemistry*, 102760 (2025).

23 Zhao, J. *et al.* A Fully Integrated and Self-Powered Smartwatch for Continuous Sweat Glucose Monitoring. *ACS Sensors* **4**, 1925-1933, doi:10.1021/acssensors.9b00891 (2019).

24 Sengupta, J. & Hussain, C. M. Mxene-based electrochemical biosensors: Advancing detection strategies for biosensing (2020–2024). *Biosensors* **15**, 127 (2025).

25 Kumar, S., Lei, Y., Alshareef, N. H., Quevedo-Lopez, M. & Salama, K. N. Biofunctionalized two-dimensional Ti3C2 MXenes for ultrasensitive detection of cancer biomarker. *Biosensors and Bioelectronics* **121**, 243-249 (2018).

26 Pan, Y., He, M., Wu, J., Qi, H. & Cheng, Y. One-step synthesis of MXene-functionalized PEDOT: PSS conductive polymer hydrogels for wearable and noninvasive monitoring of sweat glucose. *Sensors and Actuators B: Chemical* **401**, 135055 (2024).

27 Ho, T. A. *et al.* Edge-on MoS2 thin films by atomic layer deposition for understanding the interplay between the active area and hydrogen evolution reaction. *Chemistry of Materials* **29**, 7604-7614 (2017).

28 Ravitchandiran, A. *et al.* ZnFe (PBA)@ Ti3C2Tx nanohybrid-based highly sensitive non-enzymatic electrochemical sensor for the detection of glucose in human sweat. *Scientific Reports* **14**, 23835 (2024).

29 Luo, Y. *et al.* Screen-printed electrode modified with MoO3-MoS2/Ni porous array for sensitive non-enzymatic glucose sensor. *Sensors and Actuators A: Physical* **364**, 114817 (2023).

30 Huang, J., Wang, S., Ding, J., Li, S. & Xu, J. Enhanced Glucose Sensing Performance via Synergistic Integration of Silver Nanowires and Cobalt Oxide. *Surfaces and Interfaces*, 107065 (2025).

31 Bhide, A., Muthukumar, S. & Prasad, S. CLASP (Continuous lifestyle awareness through sweat platform): A novel sensor for simultaneous detection of alcohol and glucose from passive perspired sweat. *Biosensors and Bioelectronics* **117**, 537-545 (2018).

32 Shamili, C. *et al.* All-printed wearable biosensor based on MWCNT-iron oxide nanocomposite ink for physiological level detection of glucose in human sweat. *Biosensors and Bioelectronics* **258**, 116358 (2024).

33 Sempionatto, J. R., Moon, J.-M. & Wang, J. Touch-based fingertip blood-free reliable glucose monitoring: Personalized data processing for predicting blood glucose concentrations. *ACS sensors* **6**, 1875-1883 (2021).

34 Li, J., Liu, J., Wang, J., Li, W. & Wang, F. A flexible biosensor for efficiently glucose monitoring in sweat based on copper nanoparticles modified PHEMA hydrogel. *European Polymer Journal* **222**, 113630 (2025).

Author contributions

M.F designed and fabricated the smartwatch and wrote the main manuscript text. D.D is supervisor and scientific planner. M.M and Z.K prepared figures. All authors reviewed the manuscript.

Acknowledgment

This study was conducted as part of the postdoctoral program at the University of Kashan, supported by grant number 1403/4916.